

¹ **Space-Time Ambiguity Function for** ² **Electronically Scanned ISR**

John Swoboda,¹ Joshua Semeter,¹ Philip Erickson²

Corresponding author: J. P. Swoboda, Department of Electrical & Computer Engineering,
Boston University, 8 Saint Marys Street Boston, MA 02215, USA. (swoboj@bu.edu)

¹Department of Electrical & Computer
Engineering, Boston University, Boston,
Massachusetts, USA.

²Atmospheric Science Division, MIT
Haystack Observatory, Westford
Massachusetts, USA.

Electronically steerable array (ESA) technology has recently been used in incoherent scatter radars (ISR). These arrays allow for pulse-to-pulse steering of the antenna beam as opposed to a dish antenna which can only measure plasma parameters along one beam at a time. This allows for more flexibility in the measurement of ionospheric plasma parameters.

Currently these systems are operating in the high latitude region where the ionosphere is highly dynamic in both space and time. Because of the highly dynamic nature of the ionosphere in this region it is important to differentiate between artifacts and the true behavior of the plasma. Often the three dimensional data is fitted in a spherical coordinate space and then the parameters are interpolated to a Cartesian grid. This and other sources of error could be impacting the reconstructions of the plasma parameters.

To take advantage of the new flexibility of ESA system we present a new way of analyzing ISR through use of the space-time ambiguity function. This concept is similar to the range ambiguity function that is used in traditional ISR for scanning antenna systems but has been extended to all spatial dimensions along with time as well.

The use of this new ambiguity function allow us to pose this problem in terms of a linear inverse problem for the lags of the intrinsic plasma autocorrelation function. From this we can explore the impact of non-uniformity in the plasma parameters in both time and space. Along with showing possible artifacts we will begin to discuss ways of reducing these artifacts.

1. Introduction

Incoherent scatter radar (ISR) is a powerful tool for exploring the ionosphere. These systems can give measurements of electron density N_e , ion temperature T_i , electron temperature T_e , ion velocity V_i and other plasma parameters [Dougherty and Farley, 1960; Farley et al., 1961; Dougherty and Farley, 1963; Hagfors, 1961]. These parameters are measured by fitting a nonlinear theoretic autocorrelation function (ACF) model derived from first principles physics to an estimated time autocorrelation, or alternatively, the power spectrum of the radar signal scattered off of random electron density fluctuations [Lehtinen and Huuskonen, 1996].

This is an estimation of a second order statistic of an inherently random process of scattering from electrons. In order to get an estimate of the ACF with reasonable statistical properties numerous pulses have to be averaged together. With traditional dish antennas the ISR system would build these statistics in a limited number of ways. One method consists of pointing the radar beam in a specific direction and hold it there until enough pulses were integrated to get the desired statistics. Alternatively, the beam could be scanned through a field of view and collect pulses while moving. These techniques have an implicit assumption about the uniformity of the plasma parameters within the beam while pulses are being integrated. This leads to the assumption of the stationarity of the ACF within a time and spatial resolution of the radar.

In many cases, especially in the high latitude ionosphere, this stationarity assumption is not met. Phenomena such as polar cap patches that may be moving

through the field of view at very high speeds and may only be within the beam for a short period of time [Dahlgren *et al.*, 2012a]. Poleward Boundary intensifications also can break these assumptions due to the two dimensional structure [Zesta *et al.*, 2006, 2002].

Recently electronically scannable array (ESA) technology has started to be leveraged by ISR community. The Advance Modular Incoherent Scatter Radar (AMISR) systems have already been deployed both at the Poker Flat Alaska (PFISR) and Resolute Bay Canada (RISR) [ami, 2014]. The EISCAT-3D project is currently being developed using phased array technology as well and will be capable of multi-static processing [eis, 2005]. These new systems are already being used in a number of different ways including creating volumetric reconstructions of plasma parameters [Semeter *et al.*, 2009; Nicolls and Heinzelman, 2007; Dahlgren *et al.*, 2012a, b]. These reconstructions mainly consist of taking ISR data after parameters have been fit in a spherical coordinate system and then interpolate them into a Cartesian space.

These new ESA based systems differentiate themselves from dish antennas in a fundamental way. Instead of dwelling in a single beam or scanning along a prescribed direction, an ESA can move to a different beam position within its field of view on a pulse by pulse basis. This yields a new flexibility to integrate not only along time but in space in an arbitrary direction. This can help to relax the assumption of stationarity in that now the plasma can move into a different beam and have the returns from the same plasma be integrated together. As opposed to the case with a

dish antenna where the returns from different plasma would be improperly averaged together.

In order to take advantage of this new flexibility we will put forth the idea of the space-time ambiguity function. This concept extends the range ambiguity to all three spatial dimensions along with time. In the end this ambiguity can be represented as kernel in a Fredholm integral equation,

$$\rho(\mathbf{r}_s) = \int K(\mathbf{r}_s, \mathbf{r}) R(\mathbf{r}) d\mathbf{r} \quad (1)$$

where, for ISR, $R(\mathbf{r})$ is the lag of the autocorrelation function at a specific time and position.

By using this formulation many parallels between ISR and classic camera blurring problems can be made. In cameras blurring can take place when an object moves over a space covered by one pixel while the shutter is open and the CCD is collecting photons. A diagram of this can be seen in Figure 1. The same holds for ISR except that the pixels are no longer square and instead are determined by the beam shape and pulse pattern. This is shown in the diagrams in Figure 2.

In this publication we will describe a model for the full space-time ambiguity function for ISR systems. The impact of the three-dimensional ambiguity on moving plasma will be shown through specific cases related to the polar cap patches. A simulation of a polar cap patch using a full ISR simulator, which creates ISR data at the IQ level, will be shown. Lastly possible mitigation techniques will be explored.

2. Space-Time Ambiguity

The space-time ambiguity can be thought of as a kernel to a combined volume and time integration operator. As such definitions of space and time coordinates are needed.

First a three dimensional coordinate system is defined as $\mathbf{r} = [x, y, z]^T$. For this coordinate system, $\mathbf{r} = [0, 0, 0]^T$ at the location of the radar and thus $r = |\mathbf{r}|$, also known as the range variable. This allows for the use of polar coordinates $\mathbf{r} = [r, \theta, \phi]^T$ where θ is the physical elevation angle, ϕ is the physical azimuth angle.

The radar will sample this space into a set of discrete points which will be referred to as $\mathbf{r}_s = [x_s, y_s, z_s]^T$ along with the discretized range $r_s = |\mathbf{r}_s|$. The sampled space will consist of a number of points which are the combinations of range gates and number of beams. These points can also be referred in the polar coordinates $\mathbf{r}_s = [r_s, \theta_s, \phi_s]^T$, where θ_s is the sampled elevation angle, ϕ_s is the sampled azimuth angle.

For notation purposes we use two different sets of time commonly known in radar literature as fast-time, n and slow-time, t [Richards, 2005]. Fast-time is used to describe processes with correlation time less than one pulse repetition interval (PRI). Slow-time will be used for processes that decorrelate in time on the order of the system's PRI. In order to form estimates of the ACFs, with desired statistical properties, it is assumed that the plasma parameters will change on the order of many tens to hundreds of PRIs. Generally for incoherent scatter in the E-region of

the ionosphere and above the decorrelation time is less than a PRI, thus the ACFs are formed over fast-time.

The terms n and t will represent continuous variables while n_s and t_s will be the fast time and slow time parameters sampled by the radar. The sampling rate of n_s will be the sampling rate of the A/D converters. The sampling of t_s can at the highest rate, be the PRI and at lowest, sampled once in a non-coherent processing interval (NCPI), or a period of time it takes the radar to average the desired number of pulses.

2.1. Derivation

The basic physical mechanism behind ISR is that electron density fluctuations in the ionosphere, $n_e(\mathbf{r}, n)$, scatter radio waves which can be observed by the receiver system of the radar [Dougherty and Farley, 1960]. The emitted radar signal at the transmitter will have a pulse shape $s(n)$ modulated at a central frequency that results in a scattering wave number \mathbf{k} . Using the Born approximation the signal received at time n , $x(n)$, can be represented as the following

$$x(n) = h(n) * \int e^{-j\mathbf{k}\cdot\mathbf{r}} \left(n - \frac{2r}{c} \right) n_e(\mathbf{r}, n) d\mathbf{r}, \quad (2)$$

where $h(n)$ is the receiver filter and the $*$ represents the convolution operator. In modern ISR systems this signal $x(n)$ is then sampled at discrete points in fast-time which will be referred to as n_s . The convolution and sampling operation can be brought in the integral as the following,

$$x(n_s) = \int e^{-j\mathbf{k}\cdot\mathbf{r}} s\left(n - \frac{2r}{c}\right) n_e(\mathbf{r}, n) h(n_s - n) d\mathbf{r} dn \quad (3)$$

124 Once the signal has been received and sampled the autocorrelation function is
 125 then estimated from the sampled signal $x(n_s)$. The full expression of the underlying
 126 autocorrelation of this signal is the following,

$$\begin{aligned} \langle x(n_s) x^*(n'_s) \rangle &= \int e^{-j\mathbf{k}\cdot(\mathbf{r}'-\mathbf{r})} s\left(n - \frac{2r}{c}\right) s^*\left(n' - \frac{2r'}{c}\right) \\ &\quad h(n_s - n) h(n'_s - n') \langle n_e(\mathbf{r}, n) n_e^*(\mathbf{r}', n') \rangle d\mathbf{r} d\mathbf{r}' dn dn', \quad (4) \end{aligned}$$

127 where r' is the magnitude of the vector \mathbf{r}' . By assuming stationarity of second order
 128 signal statistics along fast time, we can then substitute the the lag variables $\tau \equiv n' - n$,
 129 and $\tau_s \equiv n'_s - n_s$. With these substitutions Equation 4 becomes

$$\begin{aligned} \langle x(n_s) x^*(n_s + \tau_s) \rangle &= \int e^{-j\mathbf{k}\cdot(\mathbf{r}'-\mathbf{r})} s\left(n - \frac{2r}{c}\right) s^*\left(n + \tau - \frac{2r'}{c}\right) \\ &\quad h(n_s - n) h(n_s + \tau_s - n - \tau) \langle n_e(\mathbf{r}, n) n_e^*(\mathbf{r}', n + \tau) \rangle d\mathbf{r} d\mathbf{r}' dn d\tau \quad (5) \end{aligned}$$

130 We can make a simplifying assumption at this point that the space-time autocorre-
 131 lation function of $n_e(\mathbf{r}, t)$, $\langle n_e(\mathbf{r}, n) n_e(\mathbf{r}', n + \tau) \rangle$, will go to zero as the magnitude of
 132 $\mathbf{y} \equiv \mathbf{r}' - \mathbf{r}$ increases beyond the debye length[Farley, 1969]. Thus the rate that the
 133 spatial autocorrelation goes to zero will be such that $\tau \gg \frac{2\|\mathbf{y}\|}{c}$ thus in the argument
 134 of the pulse shape $r \approx r'$. This allows Equation 5 to be rewritten as

$$\langle x(n_s)x^*(n_s + \tau) \rangle = \int s \left(n - \frac{2r}{c} \right) s^* \left(n + \tau - \frac{2r}{c} \right) h(n_s - n) h^*(n_s + \tau_s - n - \tau) \left[\int e^{-2j\mathbf{k} \cdot \mathbf{y}} \langle n_e(\mathbf{r}, n) n_e^*(\mathbf{y} + \mathbf{r}, n + \tau) \rangle d\mathbf{y} \right] d\mathbf{r} dn d\tau. \quad (6)$$

The inner integral is a spatial Fourier transform evaluated at the wave number of the radar \mathbf{k} . By again asserting stationarity along slow time we can represent the true ACF as the following,

$$R(\tau, \mathbf{r}) = \langle |n_e(\mathbf{k}, r, \tau)|^2 \rangle \equiv \int e^{-2j\mathbf{k} \cdot \mathbf{y}} \langle n_e(\mathbf{r}, b) n_e^*(\mathbf{y} + \mathbf{r}, n + \tau) \rangle d\mathbf{y}. \quad (7)$$

Now Equation 6 becomes

$$\langle x(n_s)x^*(n_s + \tau_s) \rangle = \int \langle |n_e(\tau, \mathbf{k}, \mathbf{r})|^2 \rangle \left[\int s \left(n - \frac{2r}{c} \right) s^* \left(n + \tau - \frac{2r}{c} \right) h(n_s - n) h^*(n_s + \tau_s - n - \tau) dn \right] d\tau dr. \quad (8)$$

If n_s is replaced with $2r_s/c$ we can introduce the range ambiguity function $W(\tau_s, r_s, \tau, r)$ by doing the following substitution,

$$W(\tau_s, r_s, \tau, r) = \int s \left(n - \frac{2r}{c} \right) s^* \left(n + \tau - \frac{2r}{c} \right) h(2r_s/c - n) h^*(2r_s/c + \tau_s - n - \tau) dn. \quad (9)$$

Assuming, for the moment, that $R(\tau, \mathbf{r})$ only varies across the range dimension r

we can now represent this in the form of a Fredholm integral equation

$$\langle x(2r_s/c)x^*(2r_s/c + \tau_s) \rangle = \int W(\tau_s, r_s, \tau, r) R(\tau, r) dr d\tau. \quad (10)$$

The range ambiguity function, $W(\tau_s, r_s, \tau, r)$, can be thought of as a smoothing operator along the range and lag dimensions of $R(\tau, r)$.

The spatial ambiguity across the azimuth and elevation angles is determined by the antenna beam pattern. In phased array antennas this beam pattern is ideally the array factor multiplied by the element pattern [Balanis, 2005]. The array factor is determined by a number of things including the element spacing in both x and y (dx, dy) and the wave number of the radar, k . For example, by making idealized assumptions with no mutual coupling and that the array elements are cross dipole elements, AMISR systems will have the following antenna pattern for pointing angle (θ_s, ϕ_s) ,¹

$$F(\theta_s, \phi_s, \theta, \phi) = \frac{1}{2}(1 + \cos(\theta)^2) \left[\frac{1}{MN} (1 + e^{j(\psi_y/2 + \psi_x)}) \frac{\sin((M/2)\psi_x)}{\sin(\psi_x)} \frac{\sin((N/2)\psi_x)}{\sin(\psi_x/2)} \right]^2, \quad (11)$$

where $\psi_x = -kd_x(\sin \theta \cos \phi - \sin \theta_s \cos \phi_s)$, $\psi_y = -kd_y(\sin \theta \sin \phi - \sin \theta_s \sin \phi_s)$ and M is the number of elements in the x direction of the array, and N is the number of elements in the y direction(see Appendix: A for derivation).

The spatial ambiguity is a separable function made up of the components of $W(\tau_s, \tau, r_s, r)$ and $F(\theta_s, \phi_s, \theta, \phi)$. These two functions can be combined by multiplying the two, creating the spatial ambiguity function $K(\tau_s, \mathbf{r}_s, \tau, \mathbf{r})$, and then doing a volume integration. This will create radar system's estimate of the ACF using one pulse which will be referred to as $\rho(\tau_s, \mathbf{r}_s)$,

$$\rho(\tau_s, \mathbf{r}_s) = \int F(\theta_s, \phi_s, \theta, \phi) W(\tau_s, r_s, \tau, r) R(\tau, \mathbf{r}) dV, \quad (12)$$

$$= \int K(\tau_s, \mathbf{r}_s, \tau, \mathbf{r}) R(\tau, \mathbf{r}) dV. \quad (13)$$

A rendering of an example of this full spatial ambiguity function for an uncoded long pulse and antenna pattern in Equation 11 for four beams can be seen in Figure 3.

This one pulse is a single sample of a random process. In order to create a usable estimate multiple samples of this ACF need to be averaged together to reduce the variance to sufficient levels in order to fit the estimate to a theoretical ACF that is tied to plasma parameter values. To show the impact of this averaging to create the estimate of the ACF we will add slow-time dependence to $R(\tau, \mathbf{r}, t)$ along with another separable function $G(t_s, t)$ to the kernel. This function $G(t_s, t)$, while reducing the variance can create blurring of the ACF if the plasma parameters change within a NCPI. Since the radar is sampling the space with individual pulses this function can take the form of a summation of Dirac delta functions

$$G(t_s, t) = \sum_{j=0}^{J-1} \alpha_j \delta(t - t_s - jT_{PRI}), \quad (14)$$

where J is the number of pulses used over a NCPI, T_{PRI} is the PRI time period and α_j is the weights that the radar assigns to the pulses. The weights are generally set to $1/J$ to simply average the pulses. With Equation 14 incorporated into the overall ambiguity we see the full integral equation,

$$\rho(\tau_s, \mathbf{r}_s, t_s) = \int G(t_s, t) K(\tau_s, \mathbf{r}_s, \tau, \mathbf{r}) R(\tau, \mathbf{r}, t) dV dt \quad (15)$$

$$\rho(\tau_s, \mathbf{r}_s, t_s) = \int L(\tau_s, \mathbf{r}_s, t_s, \tau, \mathbf{r}, t) R(\tau, \mathbf{r}, t) dV dt. \quad (16)$$

The final kernel, $L(\tau_s, \mathbf{r}_s, t_s, \tau, \mathbf{r}, t)$ encompasses the full space-time ambiguity.

2.2. Ambiguity after Frame Transformation

We will now focus on the impact of the motion of plasma as it is going through the field of view of the radar. We will assume that the radar is integrating over a length of time T beginning at t_s . The kernel L will be represented as a separable function K and G as in Equation 15. In this case G will be a summation of Dirac delta functions with weights of $1/J$. This will change Equation 15 to the following,

$$\rho(\tau_s, \mathbf{r}_s, t_s) = \int K(\tau_s, \mathbf{r}_s, \tau, \mathbf{r}) \left[(1/J) \int_{t_s}^{t_s+T} \sum_{j=0}^{J-1} \delta(t - t_s - jT_{PRI}) R(\tau, \mathbf{r}, t) dt \right] dV. \quad (17)$$

Of specific interest are instances in the high latitude ionosphere where embedded plasma structures are moving due to the electric field of the magnetosphere. Because of this it will be assumed that the plasma is a rigid object and will not deform with respect to \mathbf{r} over time period $[t_0, t_0 + T]$ where $T = JT_{PRI}$ is the time for one NCPI. Also it will be assumed that it will be moving with a constant velocity \mathbf{v} . Thus $R(\tau, \mathbf{r}, t) \Rightarrow R(\tau, \mathbf{r} + \mathbf{v}t)$. The assumption of rigidity is possible to make over the time period of the NCPI, on the order of a few minutes, while the plasma moves through the field of view of the radar. One example can be taken from the high latitude ionosphere while large scale features in structures such as patches decay on the order of hours [Tsunoda, 1988]. This assumption is useful because it shows the utility of this frame work to analyze the impacts on the true resolution of the ISR systems. With these assumptions Equation 17 becomes,

$$\rho(\tau_s, \mathbf{r}_s, t_s) = (1/J) \int \int_{t_s}^{t_s+T} \sum_{j=0}^{J-1} \delta(t - t_s - jT_{PRI}) K(\tau_s, \mathbf{r}_s, \tau, \mathbf{r}) R(\tau, \mathbf{r} + \mathbf{v}t) dt dV \quad (18)$$

181 A change of variables to $\mathbf{r}' = \mathbf{r} + \mathbf{v}t$ acts as a Galilean transform and applies a
 182 warping to the kernel, changing the frame of reference. Since $R(\tau, \mathbf{r}')$ is no longer
 183 dependent on t Equation 18 becomes,

$$\rho(\tau_s, \mathbf{r}_s, t_s) = (1/J) \int \left[\sum_{j=0}^{J-1} K(\tau_s, \mathbf{r}_s, \tau, \mathbf{r}' - \mathbf{v}(t_s + jT_{PRI})) \right] R(\tau, \mathbf{r}') dV. \quad (19)$$

184 By performing the integration in t the problem can now be simplified further back
 185 to a Fredholm integral equation by simply replacing the terms in the square brackets
 186 as a new kernel $A(\tau_s, \mathbf{r}_s, t_s, \tau, \mathbf{r}')$,

$$\rho(\tau_s, \mathbf{r}_s, t_s) = \int A(\tau_s, \mathbf{r}_s, t_s, \tau, \mathbf{r}') R(\tau, \mathbf{r}') dV. \quad (20)$$

187 The impact of the plasma velocity on the ambiguity function can be seen in Figure
 188 4. This is the same ambiguity as seen in Figure 3 but with a velocity of 500 m/s in
 189 the y direction over a period of 2 minutes. This velocity creates a larger ambiguity
 190 function in the frame of reference of the moving plasma.

191 The operator A can be determined through knowledge of the radar system's beam
 192 pattern along with the experiments pulse pattern, integration time and velocity of
 193 the plasma. This velocity \mathbf{v} can be estimated by taking measurements of the Doppler
 194 shift and using a methodology seen in [Butler *et al.*, 2010]. Once the operator has

been determined standard processing techniques can be used as if the plasma is not moving, under the previous assumptions.

3. Simulation

Although Figures 3 and 4 show the spatial extent of the space-time ambiguity function both with and without target motion, the impact of this on the reconstruction data can better shown through simulation. To do so we show data from a 3-D ISR simulator with a known ionosphere. In the following section we describe this simulator along with two case studies to show the impact of this ambiguity on properly reconstructing the parameters in the ionosphere.

3.1. Simulator

The simulator creates data by deriving time filters from the autocorrelation function and applying them to complex white Gaussian noise generators. Stating this in another way, every point in time and space has a noise plant and filter structure as in Figure 5. The data is then scaled and summed together according to its location in range and angle space to radar. For this simulation the data points are only used if they are within 1.1° of the center beam which is a simplification of the AMISR beam pattern.

After the IQ data has been created it is processed to create estimates of the ACF at desired points of space. This processing a follows flow chart seen in Figure 6.

The sampled I/Q can be represented as $x(n_s) \in \mathbb{C}^N$ where N is the number of samples in an inter pulse period. At this point the first step in estimating the auto-

correlation function is taken. For each range gate $m \in 0, 1, \dots, M-1$ an autocorrelation is estimated for each lag of $l \in 0, 1, \dots, L-1$. This operation of forming the ACF estimates repeats for each pulse, $j \in 0, 1, \dots, J-1$, and is then summed over the J pulses. The entire operation to form the initial estimate of $\hat{R}(m, l)$ is the following,

$$\hat{R}(m, l) = \sum_{j=0}^{J-1} x(m - \lfloor l/2 \rfloor, j) x^*(m + \lceil l/2 \rceil, j). \quad (21)$$

The case shown in Equation 21 is a centered lag product, other types of lag product calculations are available but generally a centered product is used. In the centered lag product case range gate index m and sample index n can be related by $m = n_s - \lfloor L/2 \rfloor$ and the maximum lag and sample relation is $M = N - \lceil L/2 \rceil$.

After the lag products have been formed an estimate of the noise correlation is subtracted out of $\hat{R}(m, l)$, which is defined as $\hat{R}_w(m, l)$,

$$\hat{R}_w(m_w, l) = \sum_{j=0}^{J-1} w(m_w - \lfloor l/2 \rfloor, j) w^*(m_w + \lceil l/2 \rceil, j), \quad (22)$$

where $w(n_w)$ is the background noise process of the radar. Often the noise process is sampled during a calibration period for the radar when nothing is being emitted.

The final estimate of the autocorrelation function after the noise subtraction and summation rule will be represented by $\hat{R}_f(m, l)$. At this point a summation rule is applied and the data is sent off to be fit. The final parameters are derived through a standard Levenberg-Marquart non-linear least-squares fitting of n_e, T_i, T_e [Levenberg, 1944].²

3.2. Case 1

The first example is a simple case of a small plasma enhancement moving through the radar field of view. This case is meant to model conditions expected in the polar cap ionosphere under southward IMF conditions [Dahlgren *et al.*, 2012b]. The background electron density varies in altitude as a Chapman function, shown in Figure 7, while the electron and ion temperature remains constant.

Embedded in the background there is a 35 km radius sphere of enhanced electron density of $5 \times 10^{10} \text{ m}^{-3}$ centered at 400 km altitude moving at 500 m/s along the y direction. Images from this phantom can be seen in Figure 8. To simplify the simulation the atmosphere is assumed to be 100% Oxygen ions. For the ease of comparison the phantom is only shown in areas where its in the radar's field of view. The positions of the 121 beam used for this case can be seen in Figure 9.

Because only the electron density is varying the fitting method becomes simply a power estimate as the electron density is directly proportional to the return power if the temperature ration is known. This example allows the blurring from the space-time ambiguity function can be observed easier, while also showing trade offs between statistical variance and blurring. ³

Using the phantom we can see how just simply changing the integration time can impact the reconstruction. In Figure 10 we can see a case were only 10 pulses are used for the reconstruction, which corresponds to an integration time of about 9 seconds. The enhancement can be seen as it moves through the field of view although there is that there is a high amount of variance in the reconstruction. Figure 11 shows

the reconstruction with 200 pulses, 3 minute integration time. The variability has been reduced but there is a large amount of blurring of the enhancement as it moves through the field of view.

In order to give a comparison based on integration time a phantom was also created one with no motion. This can be seen in the first pane Figure 12. An image using the same integration time as in Figure 10 for the stationary phantom is the center pane in Figure 12. Another image using the longer integration time can be seen in right pane of Figure 12. These images show that the blurring is on the same order between both integration times.

3.3. Case 2

Lastly, we show results of a simulation of the plasma density enhancement through the field of view but the ion and electron temperatures are allowed to vary. We again use a plasma enhancement moving through the field of view at 500 m/s but the electron and ion temperature varies with time and altitude. The the background ion and electron temperature vs. height can be seen in Figure 14. As the electron density enhancement travels through the field of view the temperatures drop by the same ratio that the electron density is enhanced. This is done to keep the variance the same.

The phantoms for each parameter at approximately 402 seconds can be seen in Figure 14. The reconstruction of this field at the same time can be seen in Figure 15. The reconstruction does not seem to show the electron density enhancement even in a blurred form.

In order to determine the reason behind the poor reconstruction we look at the fit surface of one of the points in the reconstruction. The fit surface is the error between the estimated ISR spectrum and the spectrum derived from the different parameters. Comparing the points $\mathbf{r} = [10, 10, 400]\text{km}$ and the closest reconstruction point in the radar field of view, $\mathbf{r}_s = [6.72, 1.80, 398.77]$. The time was chosen so the integrated measurement would be centered over the time when the enhancement moved through this point. During this time period the radar will integrate over two distributions of plasma at this point. The plasma at point \mathbf{r} are $N_e = 1.96 \times 10^{10}\text{m}^{-3}$, $T_i = 1064$ °K and $T_e = 1324$ °K when there is no enhancement traveling through. When the enhancement is traveling through this point $N_e = 5 \times 10^{10}\text{m}^{-3}$, $T_i = 416$ °K and $T_e = 518$ °K. The speed of the enhancement, which is going at 500 m/s, causes about two-thirds of the pulses to correspond to the enhanced plasma during the integration.

The fit results in the parameter values at \mathbf{r} are $N_e = 2.36 \times 10^{10}\text{m}^{-3}$, $T_i = 973$ °K and $T_e = 500$ °K. The fit surface was formed over the parameter space of N_e 1×10^{10} to $1 \times 10^{11}\text{m}^{-3}$, and for both T_e and T_i were over an values 100 to 1500 °K. In this case the fit surface showed that the global minimum was located in the same found in the same location as found by the Levenberg-Marquart algorithm. . A two dimensional cut of the fit surface at $N_e = 2.43 \times 10^{10}$ and showing its variability between T_i and T_e in Figure 16. Since this is a global minimum supports the possibility of the non uniformity of the plasma parameters causing and erroneous fit. Mixtures of different plasma populations causing erroneous fits have been shown before such as in [Knudsen et al., 1993].⁴

4. Possible Mitigation Techniques

There are a number of possible ways to remove the ISR operator function to the data. A relatively simply way to remove the problem is to process the data in the frame of reference of the plasma. Already it has been shown that it is possible to measure the vector velocity of plasma flows, [Butler *et al.*, 2010]. After measuring the velocity instead of integrating in the same beam one could integrate across different beams using this knowledge. This would allow for ACF to be formed from the same populations of plasma as it moves through the field of view.

In order to reconstruct the plasma parameters it is necessary to do some sort of regularization. There are two type of regularization that can be applied in this case the first is parameter based regularization, like full profile analysis Holt *et al.* [1992]; Hysell *et al.* [2008]. The term parameter based regularization in this case means applying constraints to the physical parameters that are often determined after fitting. This can require a large amount of calculation because the fitting and constraints are done in one step. Currently full profile analysis has only been applied along the range dimension and not in all three spatial dimensions.

The other method will be referred to as data based regularization. This term infers the application of constraints to the estimates of the autocorrelation functions. The constraints usually deal with how the data changes over time and space by constraining the energy of the ACFs or its derivative. This has an advantage of being more computationally tractable in that it is now a linear inverse problem. Using the ideas stated in this paper one can cast the reconstruction of the four

dimensional function of the ACFs in these terms. The issue with doing this data based reconstruction is it is unknown how to constrain the reconstruction in the best way.

The two examples of data based regularization in the one dimensions ISR literature are lag profile inversion and deconvolution methods. Lag profile inversion creates an operator that takes the measured data from a theoretical ACFs to the measured ACFs [Virtanen *et al.*, 2008]. Along with the operator there is also an assumed Gaussian error. This error can be then estimated from the data. This Bayesian frame work can actually be rewritten as a least squares minimization along with a Tikhonov constraint. Because of this one can show that the deconvolution methods from Nikoukar *et al.* [2008] are extremely similar to lag profile inversion with differences in only what type of constraints are used.

In order to properly process data from ESA systems these methods will have to be extended to all three dimensions. Both methods have advantages and disadvantages. In data based regularization constraints must be applied to the ACFs, which yields the question of what is the most reasonable constraint to use. Although this methodology will allow researchers to use methods from linear inverse theory, which has been well studied. The parameter based regularization method allows for use of physics based constraints to reconstruct the parameters. This technique though would likely yield solutions that would be very computationally intensive compared to techniques for data based regularization. In any case, both methods requires the forward model which has been discussed in this paper.

5. Conclusion

We have presented a new method for analyzing incoherent scatter radar processing through use of the full space-time ambiguity function. This allows for taking into account the antenna beam pattern, pulse pattern and time integration. Through simulation we have shown how plasma motion can impact reconstruction of parameters which compounded with the non-linear nature of the parameter fitting step can create errors which are hard to predict. Lastly we have suggested a number of ways using three dimensional ISR systems we could mitigate these errors and reconstruct parameters at higher resolutions then what is currently possible.

Appendix A: Derivation of Idealized AMISR Array Pattern

The current antenna on the AMISR systems is made up 8x16 set of panel of half wave cross dipoles. Each panel has 32 cross dipoles in a 8x4 hexagonal configuration. In the current set up at the Poker Flat site this yields at 4096 element array in a 64x64 element hexagonal configuration.

In order to simplify the antenna can be treated as two rectangular arrays of cross dipoles interleaved together. In the x direction each of these arrays will have a spacing of $2d_x$ with $M/2$ elements. The y direction will be of length N elements and spacing d_y . Using basic planar phase array theory, [Balanis, 2005], we can start with the linear array pattern from the first array can be represented as

$$E_1(\theta, \phi) = \sum_{m=1}^{M/2} \sum_{n=1}^N e^{-j2(m-1)kd_x \sin \theta \cos \phi - j(n-1)kd_y \sin \theta \sin \phi}. \quad (\text{A1})$$

Since the second array can be thought of a shifted version of the first in the x direction

we get the following

$$E_2(\theta, \phi) = \sum_{m=1}^{M/2} \sum_{n=1}^N e^{-j(2m-1)kd_x \sin \theta \cos \phi - j(n-1/2)kd_y \sin \theta \sin \phi}. \quad (\text{A2})$$

In order to simplify notation we will make the following substitutions, $\psi_x = -kd_x \sin \theta \cos \phi$, $\psi_y = -kd_y \sin \theta \sin \phi$. Using Equations A1 and A2 we can see the following relationship,

$$E_2(\theta, \phi) = e^{j(\psi_y/2 + \psi_x)} E_1(\theta, \phi) = \sum_{m=1}^{M/2} \sum_{n=1}^N e^{-j2(m-1)\psi_x - j(n-1)\psi_y}. \quad (\text{A3})$$

Adding E_1 and E_2 together we get the following linear array pattern

$$\begin{aligned} E(\theta, \phi) &= (1 + e^{j(\psi_y/2 + \psi_x)}) \sum_{m=1}^{M/2} \sum_{n=1}^N e^{-j2(m-1)\psi_x - j(n-1)\psi_y}. \\ &= \frac{1}{MN} (1 + e^{j(\psi_y/2 + \psi_x)}) \frac{\sin((M/2)\psi_x)}{\sin(\psi_x/2)} \frac{\sin((N/2)\psi_y)}{\sin(\psi_y/2)}. \end{aligned} \quad (\text{A4})$$

Since the array is steerable this can be taken into account in the equations by simply changing the definitions of ψ_x and ψ_y to $\psi_x = kd_x(\sin \theta \cos \phi - \sin \theta_s \cos \phi_s)$, and $\psi_y = kd_y(\sin \theta \sin \phi - \sin \theta_s \sin \phi_s)$. Lastly the antenna pattern of a single cross dipole can be represented as $\frac{1}{2}(1 + \cos^2(\theta))$ [Balanis, 2005]. By taking the squared magnitude of the array factor and multiplying it with the pattern of the dipole we get Equation 11,

$$F(\theta_s, \phi_s, \theta, \phi) = \frac{1}{2}(1 + \cos(\theta)^2) \left| \frac{1}{MN} (1 + e^{j(\psi_y/2 + \psi_x)}) \frac{\sin((M/2)\psi_x)}{\sin(\psi_x)} \frac{\sin((N/2)\psi_x)}{\sin(\psi_x/2)} \right|^2. \quad (\text{A5})$$

Notes

1. I could change this to a general phase array antenna pattern.
2. I just checked my code and it seems that I did not use V_i in my fitting. If this needs to be redone please let me know.
3. I think we had a better way of stating this.
4. Feel like I need a better ending to this section.

References

- (2005), Eiscat 3d design specification document.
- (2014), Amisr overview.
- Balanis, C. A. (2005), *Antenna Theory: Analysis and Design*, Wiley-Interscience.
- Butler, T. W., J. Semeter, C. J. Heinselman, and M. J. Nicolls (2010), Imaging f
region drifts using monostatic phased-array incoherent scatter radar, *Radio Sci.*,
45(5), RS5013, doi:10.1029/2010RS004364.
- Dahlgren, H., J. L. Semeter, K. Hosokawa, M. J. Nicolls, T. W. Butler, M. G. Johnsen,
K. Shiokawa, and C. Heinselman (2012a), Direct three-dimensional imaging of polar
ionospheric structures with the resolute bay incoherent scatter radar, *Geophysical
Research Letters*, 39(5), n/a–n/a, doi:10.1029/2012GL050895.

Dahlgren, H., G. W. Perry, J. L. Semeter, J. P. St. Maurice, K. Hosokawa,
M. J. Nicolls, M. Greffen, K. Shiokawa, and C. Heinselman (2012b), Space-
time variability of polar cap patches: Direct evidence for internal plasma struc-
turing, *Journal of Geophysical Research: Space Physics*, 117(A9), A09,312, doi:
10.1029/2012JA017961.

Dougherty, J. P., and D. T. Farley (1960), A theory of incoherent scattering of
radio waves by a plasma, *Proceedings of the Royal Society of London. Series A,
Mathematical and Physical Sciences*, 259(1296), pp. 79–99.

Dougherty, J. P., and D. T. Farley (1963), A theory of incoherent scattering of radio
waves by a plasma, 3 scattering in a partly ionized gas, *Journal of Geophysical
Research*, 68, 5473.

Farley, D. T. (1969), Incoherent scatter correlation function measurements, *Radio
Sci.*, 4(10), 935–953.

Farley, D. T., J. P. Dougherty, and D. W. Barron (1961), A theory of incoherent
scattering of radio waves by a plasma ii. scattering in a magnetic field, *Proceedings
of the Royal Society of London. Series A, Mathematical and Physical Sciences*,
263(1313), pp. 238–258.

Hagfors, T. (1961), Density fluctuations in a plasma in a magnetic field, with ap-
plications to the ionosphere, *Journal of Geophysical Research*, 66(6), 1699–1712,
doi:10.1029/JZ066i006p01699.

Holt, J. M., D. A. Rhoda, D. Tetenbaum, and A. P. van Eyken (1992), Optimal
analysis of incoherent scatter radar data, *Radio Science*, 27(3), 435–447, doi:

10.1029/91RS02922.

Hysell, D. L., F. S. Rodrigues, J. L. Chau, and J. D. Huba (2008), Full profile incoherent scatter analysis at jicamarca, *Annales Geophysicae*, *26*(1), 59–75, doi: 10.5194/angeo-26-59-2008.

Knudsen, D. J., G. Haerendel, S. Buchert, M. C. Kelley, Å. Steen, and U. Brändström (1993), Incoherent scatter radar spectrum distortions from intense auroral turbulence, *Journal of Geophysical Research: Space Physics*, *98*(A6), 9459–9471, doi: 10.1029/93JA00179.

Lehtinen, M. S., and A. Huuskonen (1996), General incoherent scatter analysis and {GUISDAP}, *Journal of Atmospheric and Terrestrial Physics*, *58*(1–4), 435 – 452, doi:http://dx.doi.org/10.1016/0021-9169(95)00047-X, Selected papers from the sixth international Eiscat Workshop.

Levenberg, K. (1944), A method for the solution of certain non-linear problems in least squares, *Quarterly of Applied Mathematics*, *2*, 164–168.

Nicolls, M. J., and C. J. Heinselman (2007), Three-dimensional measurements of traveling ionospheric disturbances with the Poker Flat Incoherent Scatter Radar, *Geophysical Research Letters*.

Nikoukar, R., F. Kamalabadi, E. Kudeki, and M. Sulzer (2008), An efficient near-optimal approach to incoherent scatter radar parameter estimation, *Radio Science*, *43*(5), n/a–n/a, doi:10.1029/2007RS003724.

Richards, M. A. (2005), *Fundamentals of Radar Signal Processing*, McGraw-Hill.

Semeter, J., T. Butler, C. Heinselman, M. Nicolls, J. Kelly, and D. Hampton (2009), Volumetric imaging of the auroral ionosphere: Initial results from pfir, *Journal of Atmospheric and Solar-Terrestrial Physics*, *71*, 738 – 743, doi: 10.1016/j.jastp.2008.08.014, Advances in high latitude upper atmospheric science with the Poker Flat Incoherent Scatter Radar (PFISR).

Tsunoda, R. T. (1988), High-latitude F region irregularities: A review and synthesis, *Reviews of Geophysics*.

Virtanen, I. I., M. S. Lehtinen, and T. Nygrén (2008), Lag profile inversion method for EISCAT data analysis, *Annales . . .*

Zesta, E., E. Donovan, L. Lyons, G. Enno, J. S. Murphree, and L. Cogger (2002), Two-dimensional structure of auroral poleward boundary intensifications, *Journal of Geophysical Research: Space Physics*, *107*(A11), SIA 6–1–SIA 6–20, doi: 10.1029/2001JA000260.

Zesta, E., L. Lyons, C.-P. Wang, E. Donovan, H. Frey, and T. Nagai (2006), Auroral poleward boundary intensifications (pbis): Their two-dimensional structure and associated dynamics in the plasma sheet, *Journal of Geophysical Research: Space Physics*, *111*(A5), n/a–n/a, doi:10.1029/2004JA010640.

Acknowledgments. (Text here)

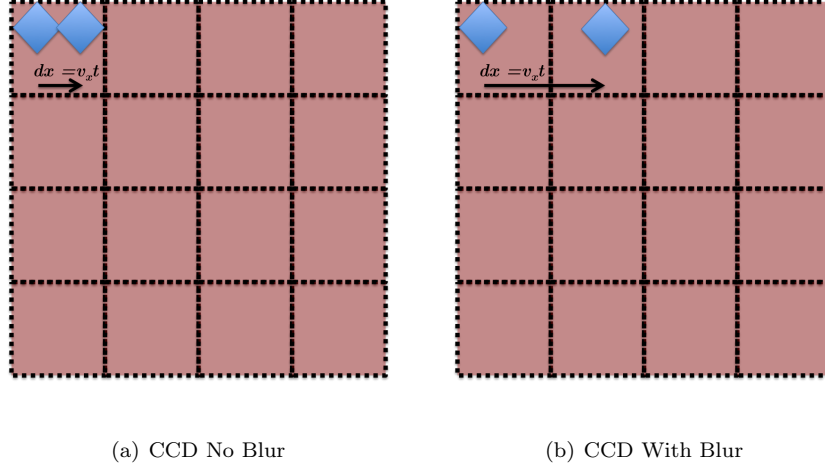


Figure 1. CCD camera

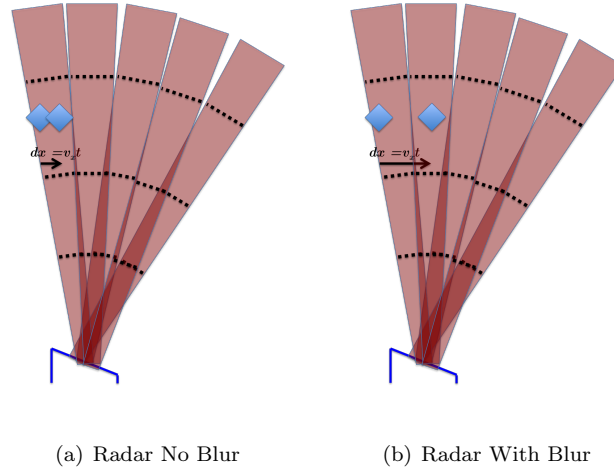


Figure 2. Radar

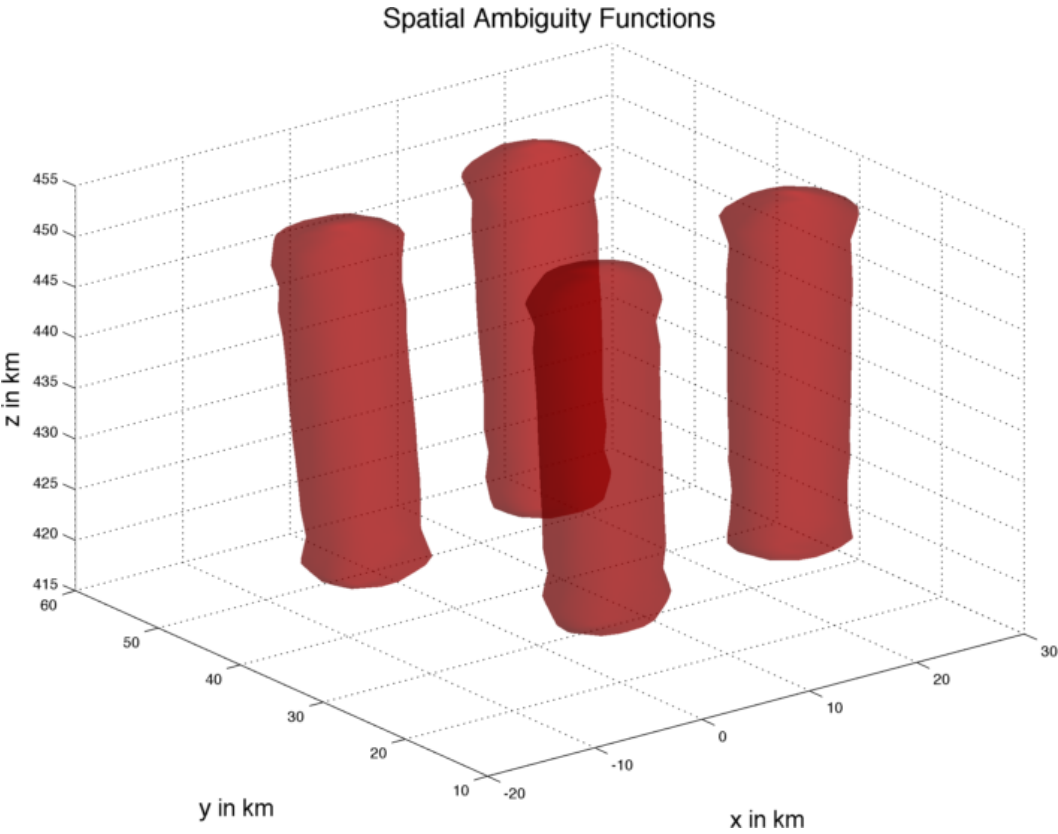


Figure 3. Full Spatial Ambiguity Function

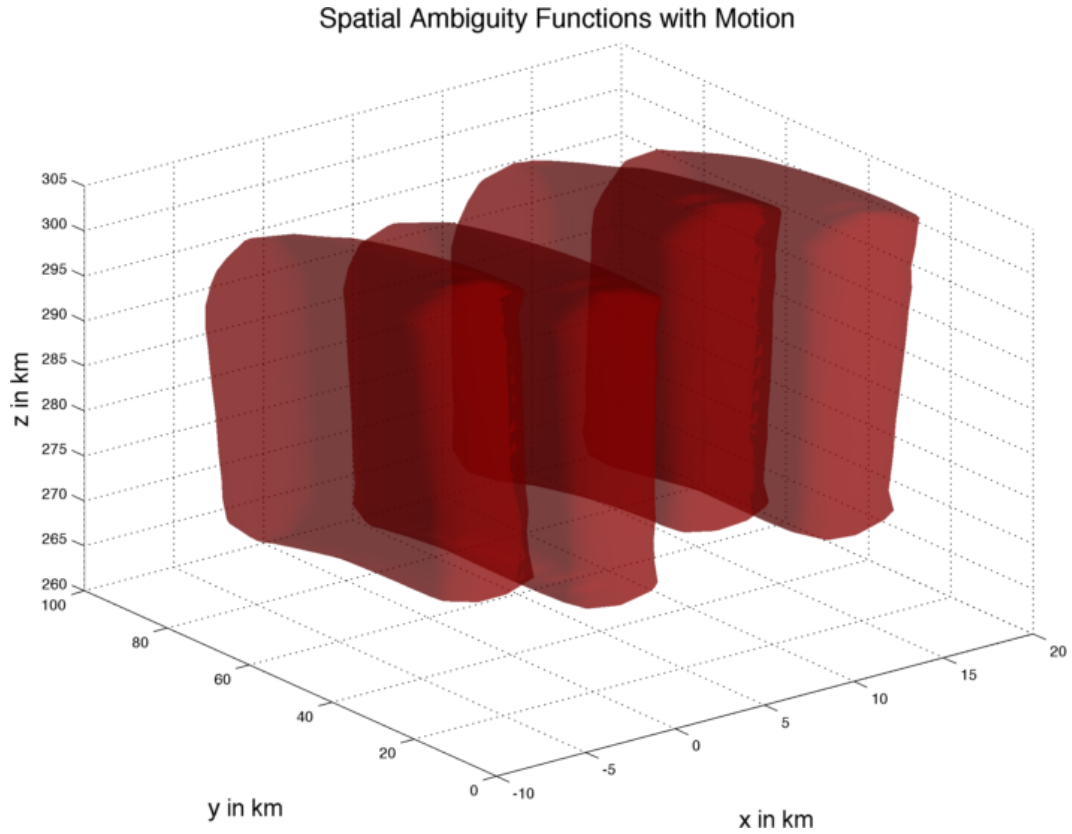


Figure 4. Full Spatial Ambiguity Function With Motion

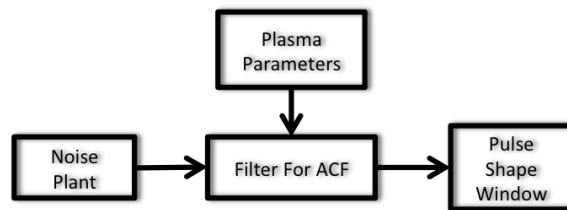


Figure 5. I/Q Simulator Diagram

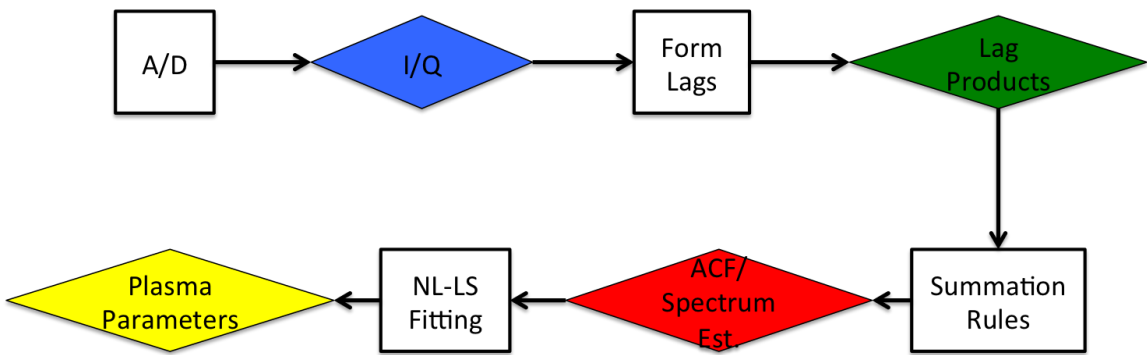


Figure 6. ISR Processing Chain.

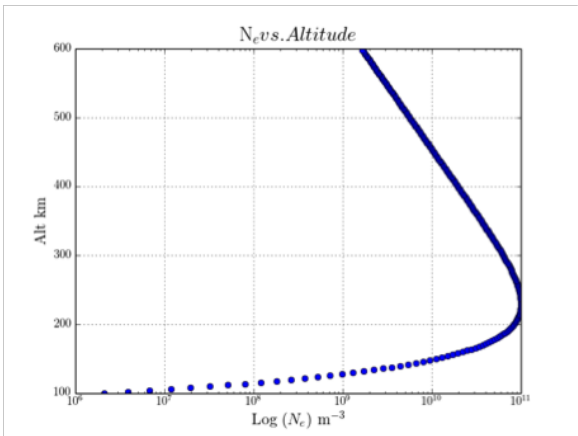


Figure 7. Electron Density vs. Altitude.

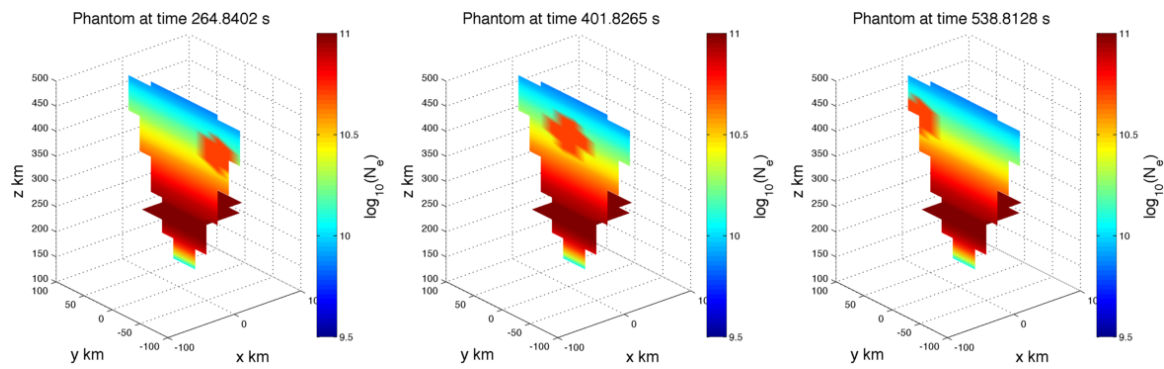


Figure 8. Images from Phantom.

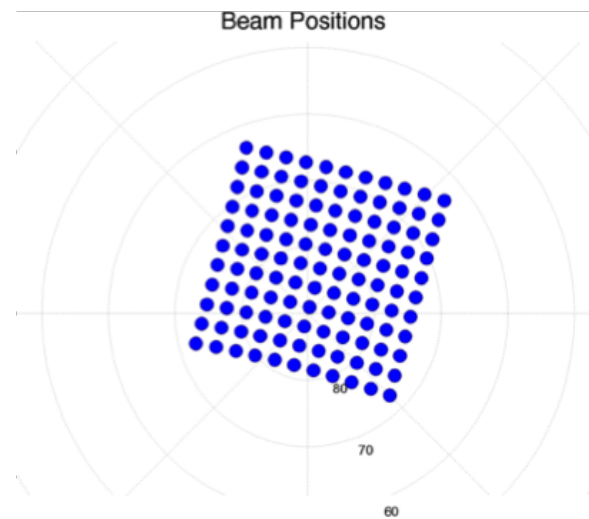


Figure 9. Beam Pattern

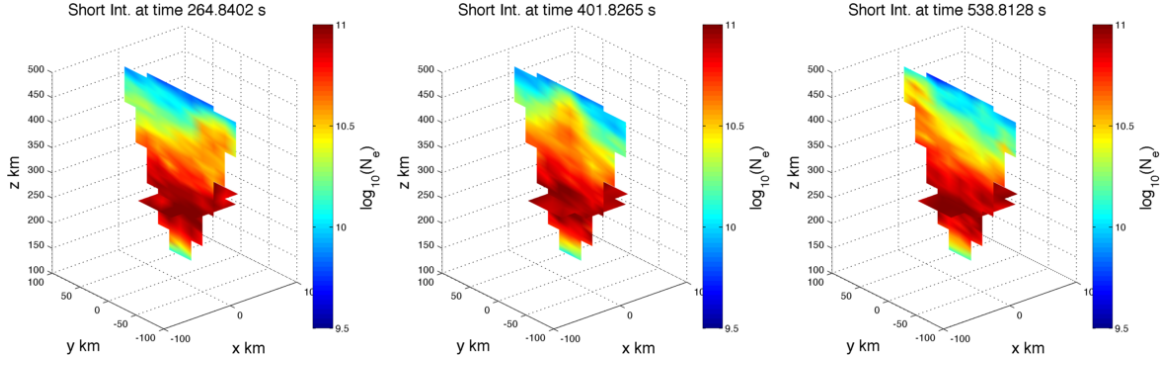


Figure 10. Images from Reconstruction Using Only 10 Pulses.

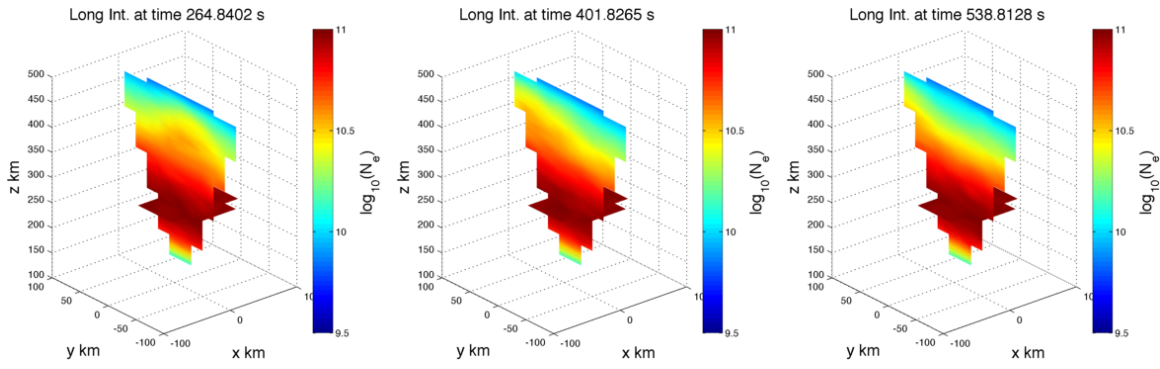


Figure 11. Images from Reconstruction Using 200 Pulses.

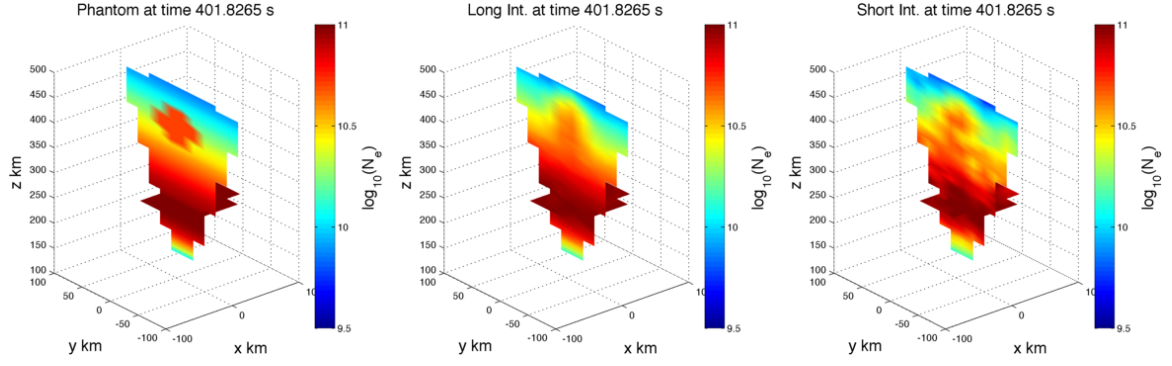


Figure 12. Stationary Phantom along with Reconstructions using 10 and 200 pulses.

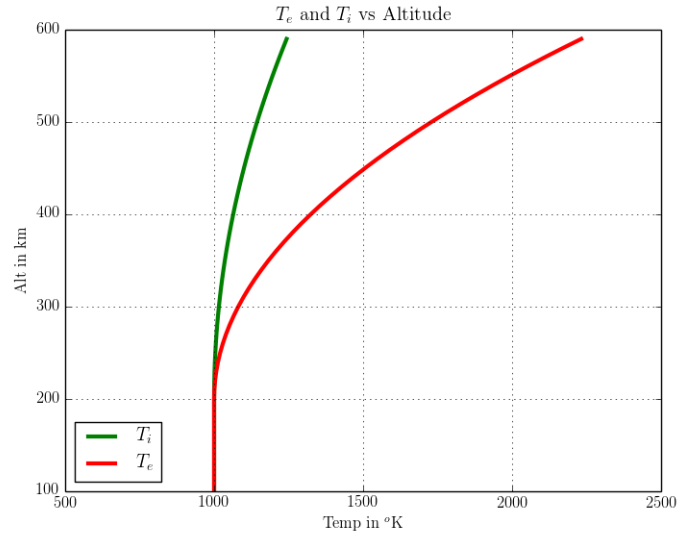


Figure 13. Ion & Electron Temperature vs. Height.

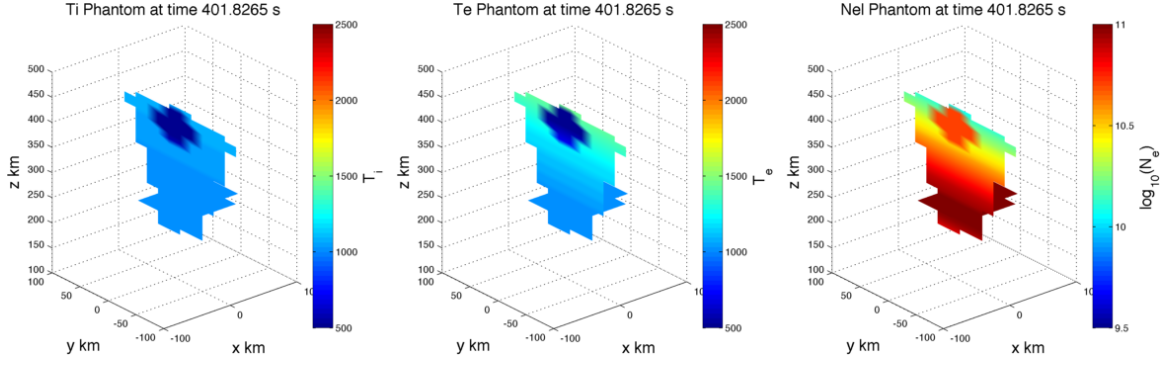


Figure 14. Phantom of Parameters.

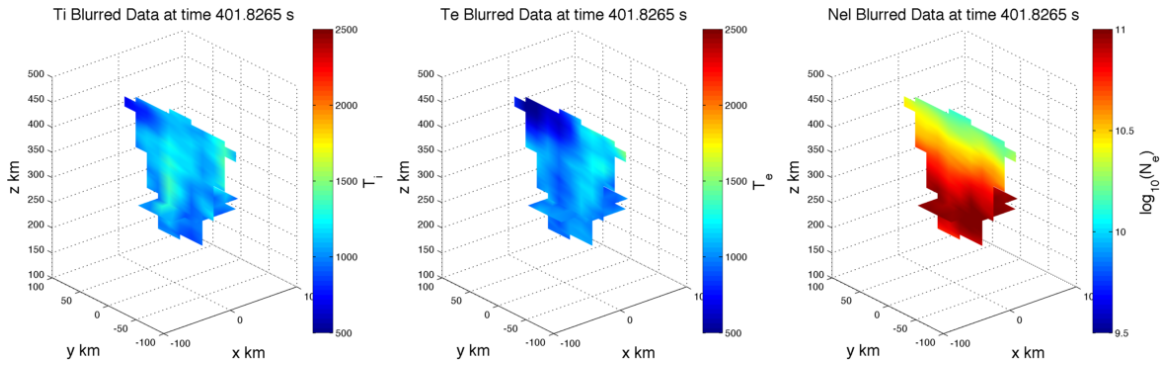


Figure 15. Interpolated Data after Full Fitting.

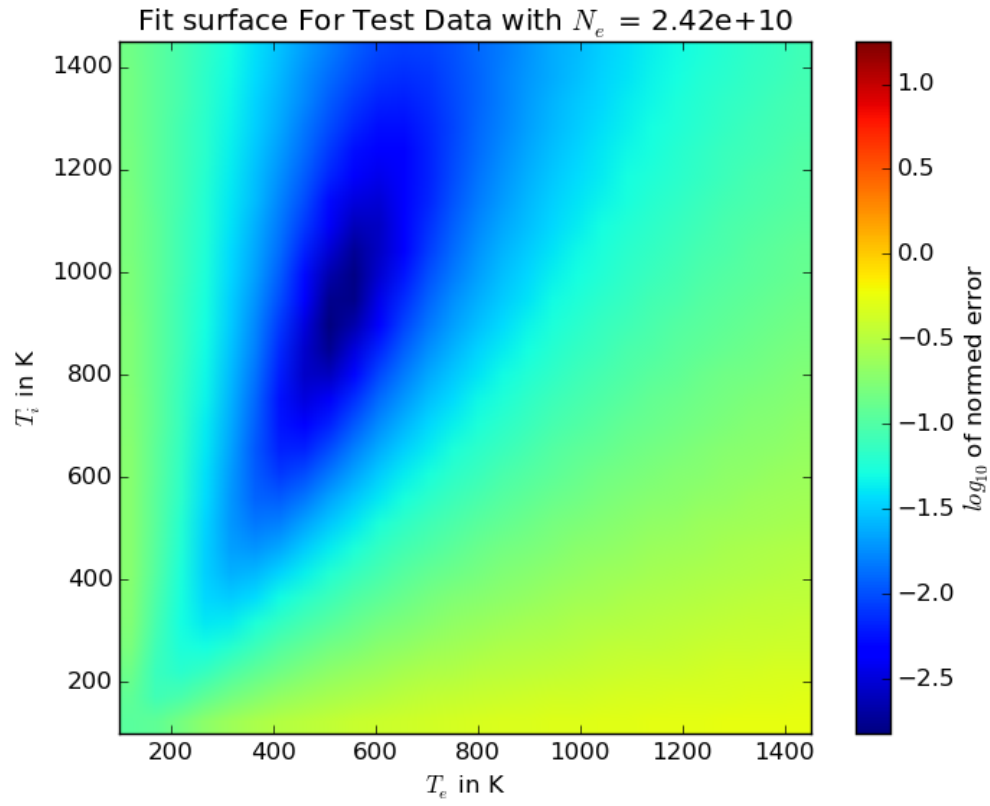


Figure 16. Fit surface.